


Cite this: *J. Mater. Chem. A*, 2022, 10, 2496

Self-assembled nano-composite perovskites as highly efficient and robust hybrid cathodes for solid oxide fuel cells†

Jun Hyuk Kim, Kyuseon Jang, Dae-Kwang Lim, Sejong Ahn, DongHwan Oh, Hyunseung Kim,  Jongsu Seo, Pyuck-Pa Choi and WooChul Jung *

The oxygen reduction reaction, which proceeds at the cathode of a fuel cell, is primarily important as its rate determines the overall performance of a device. However, designing a single-phase material that meets multiple standards (e.g., high activity, stability, and thermomechanical characteristics) at once to become an ideal cathode still remains a great challenge. In this regard, the use of multi-phase catalysts, especially those with complex nanoscale domains, may serve as a rational strategy. Here, we present $\text{Ba}_{0.5}\text{Sr}_{0.5}\text{Co}_{0.6}\text{Fe}_{0.2}\text{Zr}_{0.1}\text{Y}_{0.1}\text{O}_{3-\delta}$ (BSCFZY) as a superior biphasic nano-composite cathode, which self-assembles into two discrete cubic perovskites: Co-rich ($\text{Ba}_{0.5}\text{Sr}_{0.5}\text{Co}_{0.7}\text{Fe}_{0.2}\text{Zr}_{0.07}\text{Y}_{0.03}\text{O}_{3-\delta}$) and Zr-rich ($\text{Ba}_{0.6}\text{Sr}_{0.4}\text{Co}_{0.3}\text{Fe}_{0.2}\text{Zr}_{0.4}\text{Y}_{0.1}\text{O}_{3-\delta}$) phases. The former promotes the electrocatalytic activity while the latter supports the microstructural robustness; thus, the synergic ensemble of Co- and Zr-rich perovskite domains yields an area specific resistance of only $\sim 0.013 \Omega \text{ cm}^2$ at 650°C , which is far superior to that anticipated from the component phases in isolation. The cooperative interaction found in multi-phase catalysts prepared *via* a simple one-pot synthesis is not only attractive for SOFCs but also for other kinds of energy conversion and storage devices, such as protonic ceramic electrochemical cells, electrolyzers, and membrane chemical reformers.

Received 23rd September 2021
Accepted 21st November 2021

DOI: 10.1039/d1ta08178k

rsc.li/materials-a

1 Introduction

Catalysts address some of the most pressing societal demands, such as abatement of greenhouse gases, development of clean and efficient energy devices, and production of sustainable fuels, among others; yet the quest for finding better catalysts never ends. Amongst several strategies, the deployment of multi-phase catalysts often leads to impressive efficacy outcomes, as the advantages of the individual phases can be combined. Indeed, when materials with different functionalities come into contact, synergistic enhancement of catalysis is often observed.^{1–4} Examples can be found with CO oxidation on Pt–CeO₂,⁵ hydrogen evolution on Li⁺–Ni(OH)₂–Pt⁶ and dry methane reforming on NiFe–La_{0.6}Sr_{0.2}Ti_{0.85}Ni_{0.15}O_{2.95} perovskite oxides,⁷ among others. A phrase attributed to Aristotle, “the whole is greater than the sum of its parts”, might best suit such conditions.

The strategy has proven viable when used with a solid oxide fuel cell (SOFC) as well.⁸ As an eco-friendly power source, a SOFC represents one of the most competitive options to convert chemical fuels into electricity in a clean and sustainable

manner.^{9–14} Generally, power generation by the device hinges critically on the oxygen reduction reaction (ORR) rate; hence, a grand overarching goal for researchers has been the development of a high-performance cathode.^{15–17} For this purpose, composite electrodes have been routinely employed in the field of SOFCs, which are, in fact, a form of multi-phase catalyst. For instance, La_{0.8}Sr_{0.2}MnO₃ (LSM)-yttria-stabilized-zirconia (YSZ) is a commercially available composite cathode where each phase plays different roles; LSM acts as an electronic conducting phase and YSZ acts as an ionic conducting phase. Often, these multi-phase electrodes are prepared by physical mixing methods such as ball-milling, and even if possible, these offer only limited processability at the nanoscale. Formulating nanoscale composite electrodes has important merits, as the better homogeneity of mixing can expand the effective cathodic reaction regions, leading to a superior activity.^{18–22} Moreover, nano-structured materials endorse high porosities advantageous to the efficient gas transport. Hence, a method to obtain nano-composites is highly desirable, however often these methods are time-consuming or accompany highly energy-intensive processes, which are not practically applicable in large-scale.

In this light, nano-composites prepared *via* a self-assembly process are emerging as an attractive option, as multi-phase catalysts can be obtained by a single heat treatment at relatively low calcination temperatures.^{8,23–25} In addition to this

Department of Materials Science and Engineering, KAIST, Daejeon, Republic of Korea.
E-mail: wjchung@kaist.ac.kr

† Electronic supplementary information (ESI) available. See DOI: 10.1039/d1ta08178k

processing advantage, self-assembled materials have been found to be potential cathode candidates, evidenced by their high activity, decent chemical and physical compatibility with electrolytes, and their robust structural stability, empowered by the combination of advantageous characteristics of each distinct phase. While the design rules for the self-assembly process are not fully understood yet, as a rule of thumb, excessive B-site doping of Mo, W, Ce and Zr ions into Co and Fe-based perovskites holds high chances to yield phase separation as these elements exhibit low solid-solution compatibility.^{24,26–29} For example, Shin *et al.* carefully designed $\text{Ba}_{0.5}\text{Sr}_{0.5}(\text{Co}_{0.7}\text{Fe}_{0.3})_{0.6875}\text{W}_{0.3125}\text{O}_{3-\delta}$ (BSCFW), a composite which consists of W-rich double perovskites and W-poor single perovskites.²⁴ In this composite, W-rich double perovskites provided an inert and rigid support to active phases (*i.e.*, W-poor single perovskites), which significantly augmented the thermal stability of the material. Similarly, Song *et al.*, reported $\text{Sr}_{0.9}\text{Ce}_{0.1}\text{Fe}_{0.8}\text{Ni}_{0.2}\text{O}_{3-\delta}$ (SCFN) which consists of 4 different phases: perovskite, Ruddlesden–Popper (RP), NiO, and CeO_2 . Each domain has its characteristic role in enhancing the electrode performance;²³ the perovskite phase functions as a mixed-conducting backbone, while RP, NiO and CeO_2 promoted the oxygen bulk diffusion, oxygen surface exchange, and oxygen migration respectively. Meanwhile, Chen *et al.* reported that multi-phase catalyst coatings can dramatically improve the performance of the conventional $\text{La}_{0.6}\text{Sr}_{0.4}\text{Co}_{0.2}\text{Fe}_{0.8}\text{O}_{3-\delta}$ cathode, due to the accelerated oxygen adsorption and dissociation on $\text{BaCoO}_{3-\delta}$ nanoparticles.⁸ As shown above, self-assembled multi-phase catalysts represent salient progress toward the rational design of advanced cathodes for SOFCs.^{23,26,30,31}

Inspired by these recent advances, here we present $\text{Ba}_{0.5}\text{Sr}_{0.5}\text{Co}_{0.6}\text{Fe}_{0.2}\text{Zr}_{0.1}\text{Y}_{0.1}\text{O}_{3-\delta}$ (BSCFZY) as a self-assembled hybrid catalyst capable of rapid oxygen reaction kinetics. The composition of BSCFZY includes two paradigm-shifting cathode materials: $\text{Ba}_{0.5}\text{Sr}_{0.5}\text{Co}_{0.8}\text{Fe}_{0.2}\text{O}_{3-\delta}$ (BSCF) and $\text{BaCo}_{0.4}\text{Fe}_{0.4}\text{Zr}_{0.1}\text{Y}_{0.1}$ (BCFZY).^{32,33} BSCF is highly conducting and active toward oxygen-electrochemistry, but it comes with the caveat of questionable durability.^{24,34} On the other hand, BCFZY exhibits exceptional stability and a relatively low thermal expansion coefficient ($2.16 \times 10^{-5} \text{ K}^{-1}$), but the low electronic conductivity ($\sim 1 \text{ S cm}^{-1}$) of the material can be a concern when current collecting is not well managed.^{35,36} Hence, we make an effort to merge the key merits of these two cathodes *via* a self-assembly process. By leveraging the sinter-resistance of the Zr-containing phase, perovskites of different compositions are efficiently yielded as nano-composites within a single calcination process. The resulting multi-phase cathode demonstrates outstanding ORR performance, excellent stability, and a moderate thermal expansion coefficient mismatch to the electrolyte, suggesting that the developed material system is a highly reliable and practical candidate for use in SOFC cathodes.

2 Results and discussion

2.1 Physical characterization of BSCFZY

Fig. 1a shows the typical X-ray diffraction (XRD) profile of the as-synthesized BSCFZY obtained through a sol–gel process after

being heated at 1000°C for five hours. Based on the XRD results, the BSCFZY composite is composed of two discrete cubic perovskite oxide phases, one with larger lattice parameters ($a = 4.13 \text{ \AA}$) and the other with smaller lattice parameters ($a = 4.01 \text{ \AA}$). Additional Raman spectroscopy characterization studies revealed no specific band assignments for the BSCFZY composite, a typical feature of the cubic symmetry (Fig. S1†).¹⁹ However, the strong band feature of $\text{BaZr}_{0.8}\text{Y}_{0.2}\text{O}_{3-\delta}$ (BZY) perovskite oxides at $\nu = \sim 720 \text{ cm}^{-1}$ is not observed in the BSCFZY composite, indicating that the Zr-rich phase is not BZY.^{37,38} Rather, when compared to the XRD profiles of BSCF and BCFZY (Fig. S2†), the sample with a smaller lattice more closely approximates the composition of BSCF, while the other sample is closer to that of BCFZY.

To validate these outcomes, the BSCFZY powder was investigated using scanning transmission electron microscopy (STEM) and by means of an energy-dispersive X-ray (EDX) analysis (Fig. 1b, c, S3 and S4†). Notably, it was found that BSCFZY consists of nanograins with an inhomogeneous distribution of the Zr element according to EDX scans (Fig. 1f and g) of points 1 and 2 (Fig. 1c), signifying variations of the compositions between the two phases. Indeed, high-resolution transmission electron microscopy (HRTEM) images of each phase (Fig. 1d and e) show different diffraction planes, supporting multi-phase formation through the self-assembly process.

Although both STEM-EDX and XRD indicate the presence of two distinct phases in the powder, it is difficult to determine the accurate composition of these phases due to the overlap of EDX signals between Sr, Y, and Zr. We thus conducted atom probe tomography (APT) to investigate the composition and three-dimensional entanglement of the two phases at the atomic scale. APT is the only material analysis technique offering extensive scope for both 3D imaging and chemical measurements on the atomic scale with sub-nanometer resolutions. Details about the APT measurements are shown in Fig. S5.† Fig. 2a shows a three-dimensional atom map acquired from the BSCFZY powder. The measured bulk composition of the entire probed volume is $\text{Ba}_{0.5}\text{Sr}_{0.5}\text{Co}_{0.6}\text{Fe}_{0.2}\text{Zr}_{0.1}\text{Y}_{0.1}\text{O}_x$, in good agreement with the target composition of the as-synthesized powder. Although atoms appear to be homogeneously distributed at first glance, the cross-sectional view reveals a Co-rich phase and Zr-rich phase (Fig. 2b). The proximity histogram obtained for the upper part with respect to the iso-concentration surface of Zr of 15 at% (see Fig. 2c), *i.e.*, half of the maximum concentration of Zr in the Zr-rich phase, shows the change in elemental concentrations as a function of the distance from the boundary between Co- and Zr-rich regions (Fig. 2d). The opposed partitioning behavior of Co and Zr is consistent with the results obtained from EDX point scan analyses (Fig. 1f and g). The average compositions of the Co-rich and Zr-rich phases are analyzed as $\text{Ba}_{0.5}\text{Sr}_{0.5}\text{Co}_{0.7}\text{Fe}_{0.2}\text{Zr}_{0.07}\text{Y}_{0.03}\text{O}_x$ and $\text{Ba}_{0.6}\text{Sr}_{0.4}\text{Co}_{0.3}\text{Fe}_{0.2}\text{Zr}_{0.4}\text{Y}_{0.1}\text{O}_x$, respectively, confirming the existence of multi-phase formation in BSCFZY powder (ratio of Zr- and Co-rich phases are $\sim 11.9\%$ and $\sim 88.1\%$ respectively, as obtained from XRD analysis).

The phase structure of the self-assembled perovskites is also characterized with *in situ* high-temperature XRD (Fig. 3a).

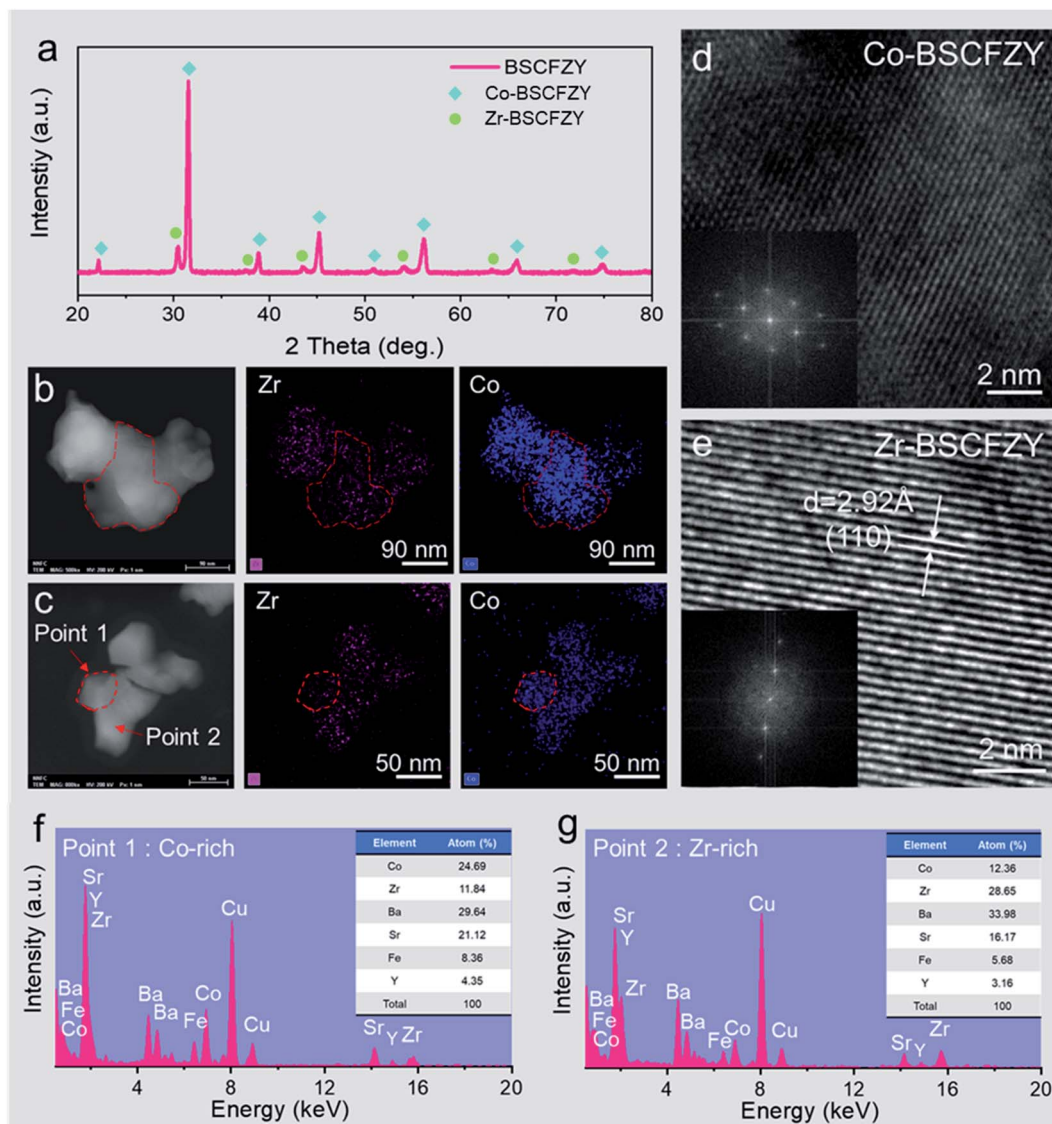


Fig. 1 Physical characterization of the self-assembled perovskites: (a) X-ray diffraction (XRD) data of the as-synthesized $\text{Ba}_{0.5}\text{Sr}_{0.5}\text{Co}_{0.6}\text{Fe}_{0.2}\text{Zr}_{0.1}\text{Y}_{0.1}\text{O}_{3-\delta}$ (BSCFZY), (b and c) STEM image and EDX mapping results of the BSCFZY sample, (d) HRTEM image of the Co-rich BSCFZY phase (Co-BSCFZY), (inset) fast Fourier transform patterns obtained from the Co-BSCFZY sample, (e) HRTEM image of the Zr-rich BSCFZY phase (Zr-BSCFZY), (inset) fast Fourier transform patterns obtained for Zr-BSCFZY, and the point EDX scanning results obtained at (f) point 1 and (g) point 2.

Under the testing conditions (*i.e.*, from room temperature to 700 °C), BSCFZY maintains its dual-phase nature, along with a slight peak shift to a lower angle. Hence the refined unit cell parameters of the Zr-BSCFZY and Co-BSCFZY phases are calculated and plotted as a function of the temperature (Fig. 3b). Due to the larger ionic radii of Zr^{4+} (86 pm) compared to those of other transition metals (Co^{3+} : 75 pm and Fe^{3+} : 78.5 pm), Zr-BSCFZY showed a larger lattice compared to that of Co-BSCFZY. As the temperature increases, the lattice expansion of both phases is observed, but with different slopes. The thermal expansion coefficients (TECs) of both phases are therefore analyzed by calculated the thermally expanded lattice parameters (Δa) divided by the lattice parameters at room temperature (a_0). The resulting TEC values are obtained and found to be $1.90 \times 10^{-5} \text{ K}^{-1}$ for Co-BSCFZY and $1.36 \times 10^{-5} \text{ K}^{-1}$ for Zr-BSCFZY.

The low TEC value of Zr-BSCFZY may be a representation of the fixed valence state of the Zr ions compared to the thermal reduction proceeding on Co/Fe ions, as shown by the thermogravimetric analysis (TGA, Fig. S6†).^{33,39} Regarding the ratio between the Zr- and Co-rich phases ($\sim 11.9\%$ and $\sim 88.1\%$ respectively), the expected TEC value for BSCFZY is $1.83 \times 10^{-5} \text{ K}^{-1}$. Although the TEC of BSCFZY could not fully match the TEC of SDC ($1.23 \times 10^{-5} \text{ K}^{-1}$) and GDC ($1.20 \times 10^{-5} \text{ K}^{-1}$),⁴⁰ compared to the conventional mixed-ionic-and-electronic-conducting cathodes which show a TEC range of $2.0\text{--}3.0 \times 10^{-5} \text{ K}^{-1}$,^{33,41–44} the TEC found for BSCFZY ($1.83 \times 10^{-5} \text{ K}^{-1}$) is quite encouraging to use in our efforts to achieve good thermo-mechanical compatibility with SOFC electrolytes.

An additional characterization of X-ray photoelectron spectroscopy (XPS) is conducted to investigate the cation

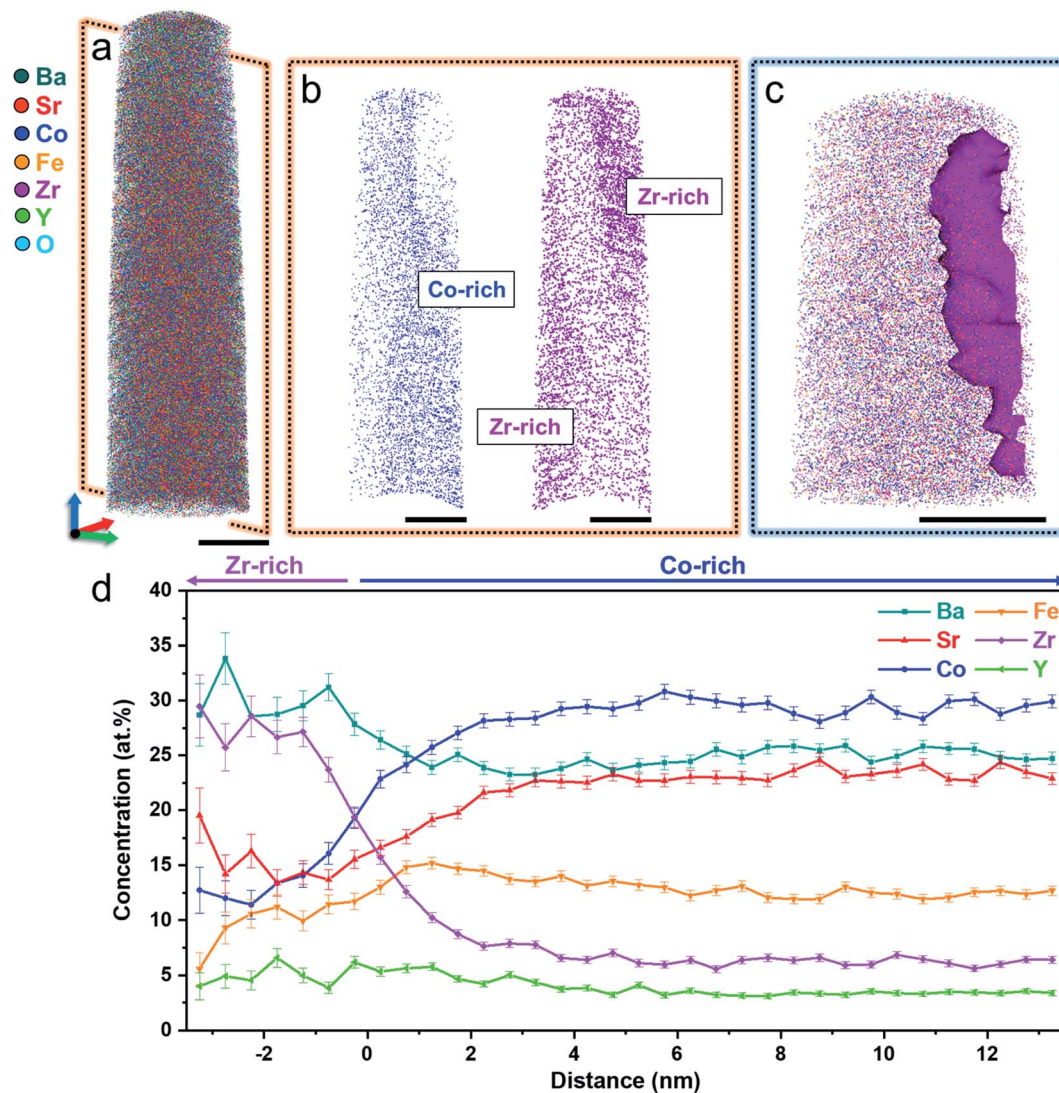


Fig. 2 Atom probe tomography (APT) analysis of the as-synthesized BSCFZY: (a) three-dimensional atom map of the BSCFZY sample. The orange dotted line indicates the cross-sectional area shown in (b). (b) Co-BSCFZY (left) and Zr-BSCFZY (right) phases visualized by the atom maps of Co and Zr, respectively. (c) Enlarged atom map of the top region with the iso-concentration surface of Zr of 15 at%. (d) Proximity histogram obtained for the iso-concentration surface shown in (c). Error bars represent a standard deviation (σ). Oxygen concentrations are not shown for clarity. (Scale bars: 20 nm).

distribution/composition on the BSCFZY surface. Fig. S7[†] shows the photoelectron spectra of constituent cations in BSCFZY. Due to the direct overlap of Co 2p and Ba 3d, we used the Co 3p spectrum instead to fit the $\text{Co}^{2+}/\text{Co}^{3+}$ ratios. Accordingly, the amounts of Co^{3+} and Co^{2+} are determined to be approximately 68 and 32%, respectively. Similarly, the Fe 3p spectrum is deconvoluted with Fe^{3+} and Fe^{2+} peaks and the corresponding amounts are thus estimated to be close to 57 and 43%. Finally, we examined the XPS spectra of Sr 3d for BSCFZY, with the doublets ($3d_{3/2}$ and $3d_{5/2}$) of both $\text{Sr}_{\text{non-lattice}}$ and $\text{Sr}_{\text{lattice}}$ assigned to deconvolute the spectra. Particularly, it is reported that the peak positions of $\text{Sr}_{\text{non-lattice}}$ appears at higher binding energies rather than those of $\text{Sr}_{\text{lattice}}$, which is an important indicator for Sr-enrichment on the perovskite surface.^{45,46} Consequently, it was found that $\text{Sr}_{\text{non-lattice}}$ is $\sim 29\%$, far lower

than $\text{Sr}_{\text{lattice}}$ ($\sim 71\%$), indicating that Sr segregation is not severe on the surface of BSCFZY. The aforementioned chemical compositions are summarized in Table S1.[†]

Other than BSCFZY, we prepared another type of self-assembled composite, $\text{Ba}_{0.5}\text{Sr}_{0.5}\text{Co}_{0.6}\text{Fe}_{0.2}\text{Ce}_{0.1}\text{Y}_{0.1}\text{O}_{3-\delta}$ (BSCFCY) *via* Ce ion doping. Similar to Zr ions, the doping of Ce ions produced separated phases, as reflected in the XRD patterns (Fig. S8[†]). However, the Co contents over the grains are rather abruptly altered (see Fig. S9[†] for a detailed characterization), indicating that the Ce-rich phase is likely $\text{BaCe}_x\text{Y}_y\text{O}_{3-\delta}$. Given that barium cerates are proton-conducting ceramics, the BSCFCY composites appear to be auspicious when applied as a protonic ceramic fuel cell (PCFC) cathode rather than being applied as a SOFC cathode (Fig. S10[†]).

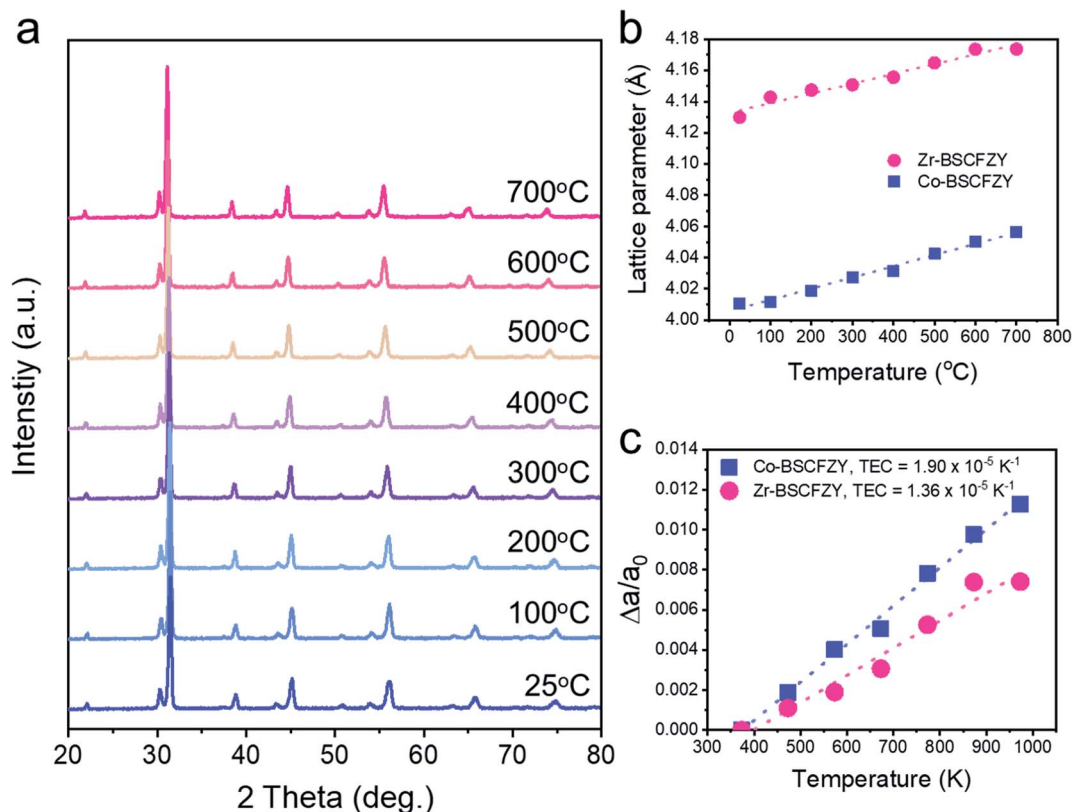


Fig. 3 (a) High-temperature X-ray diffraction (XRD) profile of $\text{Ba}_{0.5}\text{Sr}_{0.5}\text{Co}_{0.6}\text{Fe}_{0.2}\text{Zr}_{0.1}\text{Y}_{0.1}\text{O}_{3-\delta}$ (BSCFZY), (b) lattice parameter expansion of the Zr-rich BSCFZY phase (Zr-BSCFZY) and Co-rich BSCFZY (Co-BSCFZY) phase as a function of the temperature, and (c) temperature-dependence of $\Delta a/a_0$.

2.2 Electrochemical performance outcomes of the multi-phase cathodes

To elucidate the ORR catalytic activity of the BSCFZY composite, a half-cell configuration of BSCFZY|SDC|BSCFZY is initially investigated by means of electrochemical impedance spectroscopy (Fig. S11†). The interfacial polarization resistance or the area-specific resistance (ASR) is determined by subtracting the high-frequency intercept values of the impedance loop with the real axis (*i.e.*, offset resistance) from those of its low-frequency counterpart. Accordingly, the ASR of the BSCFZY cathode at 650 °C is determined to be as low as $\sim 0.013 \Omega \text{ cm}^2$ (Fig. 4a; the ASRs at lower temperatures were also collected, as shown in Fig. S12†). When compared to the parent BSCF and BCFZY cathodes, the BSCFZY composite shows a lower level of activation energy (*i.e.*, BSCF: $\sim 1.20 \text{ eV}$, BCFZY: $\sim 1.08 \text{ eV}$ and BSCFZY: $\sim 1.04 \text{ eV}$); and the absolute magnitudes of the ASRs are out-ranked at all tested temperatures (300–650 °C) (Fig. S13 and S14†). For instance, the ASRs of BSCFZY are only ~ 0.026 , 0.063 , and $0.176 \Omega \text{ cm}^2$ at 600, 550, and 500 °C, respectively. Even at lower temperatures, the ASR is less than $1 \Omega \text{ cm}^2$ at 450 °C ($0.56 \Omega \text{ cm}^2$) and less than $10 \Omega \text{ cm}^2$ at 350 °C ($7.93 \Omega \text{ cm}^2$), indicating the excellent suitability of the BSCFZY composite as a low-temperature SOFC cathode material. Furthermore, the ASR values of BSCFZY surpass those reported for benchmark multi-phase cathodes so far, such as BSCFW, $\text{Sr}_{0.9}\text{Ce}_{0.1}\text{Fe}_{0.8}\text{Ni}_{0.2}\text{O}_{3-\delta}$

(SCFN), multi-phase catalyst coated LSCF such as $\text{PrNi}_{0.5}\text{Mn}_{0.5}\text{O}_{3-\delta}$ (PNM)-LSCF and PBCC-LSCF, and Ag ex-solved $\text{Ba}_{0.95}\text{Co}_{0.8}\text{Nb}_{0.1}\text{Ta}_{0.1}\text{O}_{3-\delta}$ (Fig. 4b).^{8,19,23,24,30} A subsequent ASR stability test also demonstrated a stable behavior, highlighting the feasibility of the developed material for practical operation (Fig. S15†).

The viability of the developed composites as a PCFC cathode is additionally assessed, as parent BCFZY is a renowned cathode for PCFCs, and considerable attention has been directed at PCFCs recently due to their prospective performances at low temperatures. For this purpose, the half-cell with a symmetric configuration of BSCFZY| $\text{BaZr}_{0.1}\text{Ce}_{0.7}\text{Y}_{0.1}\text{Yb}_{0.1}\text{O}_{3-\delta}$ (BZCYYb)|BSCFZY is tested. Fig. S16† shows the half-cell results of the BSCFZY cathode based on proton-conducting electrolytes. In this case, we found a low resistance value of $\sim 0.28 \Omega \text{ cm}^2$ at 650 °C, which indicates that BSCFZY is a promising cathode candidate for PCFCs as well. Significantly, the polarization resistance of BSCFZY decreases with an increase in the water vapor pressure (Fig. S16h†), implying that BSCFZY is capable of proton conduction and therefore functions as a triple-conducting (proton, oxygen vacancy and electron-hole) oxide.

Such a high performance outcome of BSCFZY is ascribed to the intimate networking of two individual nano-crystals, which enters a cooperative partnership (Fig. 5). Because both form a mixed-ionic-and-electronic conductor, the electrochemical reduction of oxygen is expected to occur over a significant

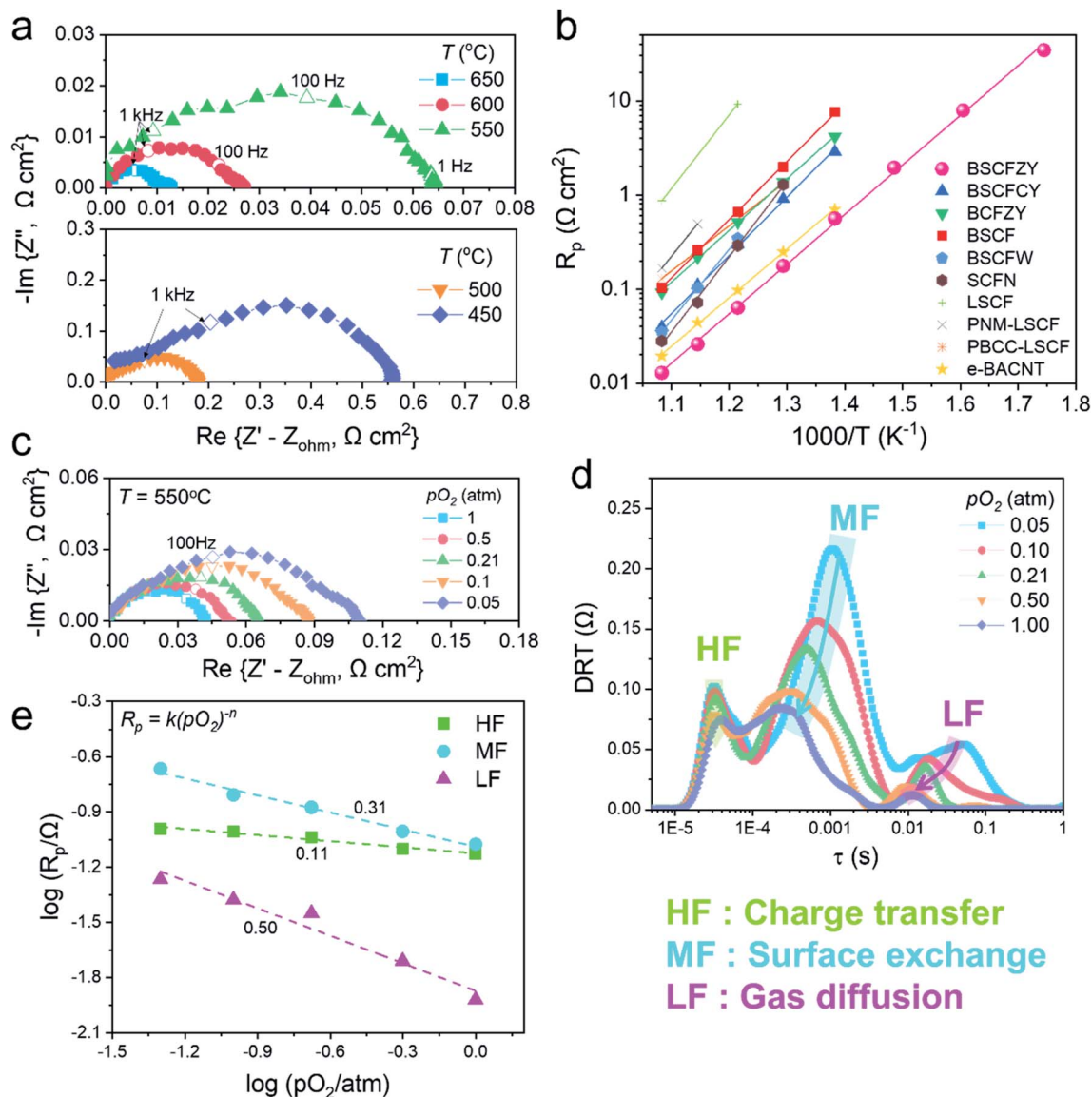


Fig. 4 (a) Electrochemical impedance spectroscopy images of porous $\text{Ba}_{0.5}\text{Sr}_{0.5}\text{Co}_{0.6}\text{Fe}_{0.2}\text{Zr}_{0.1}\text{Y}_{0.1}\text{O}_{3-\delta}$ (BSCFZY) at 450–650 °C. (b) Mapping of the oxygen reduction reaction (ORR) performance of the developed cathode over several benchmark multi-phase cathode materials as measured with a symmetric cell configuration. (c) Effects of the oxygen partial pressure on the ASRs at 550 °C. (d) According distribution of relaxation time (DRT) analyses of BSCFZY under different oxygen partial pressures at 550 °C, and (e) oxygen partial pressure dependency results at HF, MF, and LF.

portion of the electrode surface. However, the unique nano-network achieved in the form of the BSCFZY composite positively augments the ORR catalytic activity. For example, more electronically conductive Co-rich phases will aid adjacent Zr-rich phase by conductive electron-hole (h^+) transport, causing each and every part of the electrode to actively participate in the ORR. The Zr-rich phase, on the other hand, may effectively suppress the grain growth of the sinter-vulnerable Co-rich phase, hence fabricating a high-surface-area electrode that cannot be easily realized with conventional ceramic processing. In addition, Zr-rich phases can benefit stronger oxygen ion (O^{2-}) conduction due to the larger lattice parameters (Table S2†).

To determine whether the aforementioned discussions present reasonable points, a distribution of relaxation time (DRT) analysis of impedance spectroscopy is undertaken to determine possible rate-determining steps (Fig. 4c–e). The DRT analysis is a useful approach for understanding the reaction kinetics and transport phenomena of certain electrochemical systems based on the relaxation time differences among all the steps. For the ORR, the sub-processes can be largely classified into three groups: charge-transfer, surface exchange, and gas diffusion processes; Chen *et al.* proposed that each process can be attributed to the high-frequencies (HFs), mid-frequencies (MFs), and low-frequencies (LFs) of the impedance arc, respectively.^{8,16} The DRT of BSCFZY showed three distinct

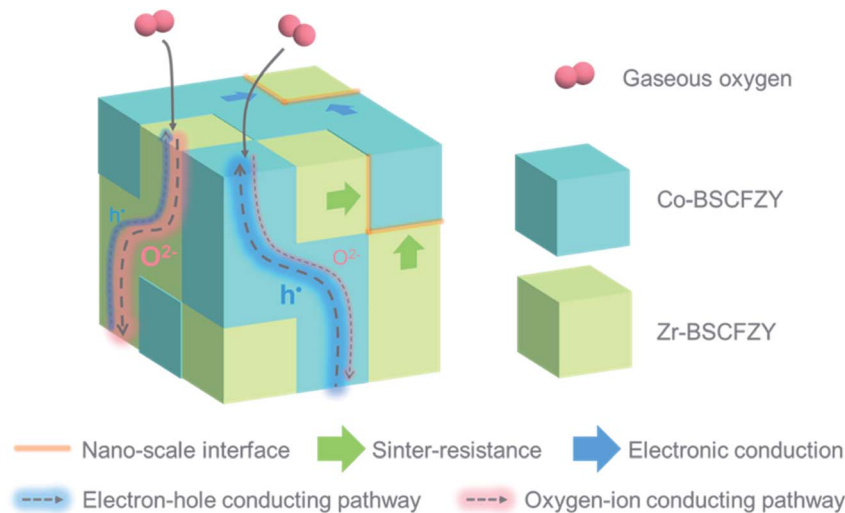


Fig. 5 Schematic representation of possible oxygen electrochemical reduction pathways of self-assembled multi-phase cathodes with a synergistic ensemble effect.

peaks, analogous to Chen's suggestion. A subsequent analysis based on the pO_2 variance (0.05–1 atm, Fig. 4d and e) and temperature dependency (Fig. S17†) over DRT functions indicated that the above assignments are convincing. For example, the most pO_2 -dependent LF process is likely associated with gaseous oxygen mass transfer processes such as diffusion, as supported by the insignificant thermal activation (Fig. S17†).^{8,19,47} On the other hand, the least pO_2 -dependent HF process is possibly the charge transfer (O^{2-}) across the electrode/electrolyte interface, and the remaining MF can be attributed to surface exchange processes, including the partial reduction of adsorbed oxygen and subsequent dissociation.^{48,49}

We then compared the EIS and related DRT functions of BSCFZY to those of BSCF, BCFZY, and the ball-milled BSCF + BCFZY composite cathode (Fig. 6a and S18†), since the compositions of the phase isolated in BSCFZY (*i.e.*, Co-BSCFZY and Zr-BSCFZY) are close enough to those of BSCF and BCFZY, respectively. The collective EIS and DRT analysis results here suggest that the Co-rich phase is responsible for facile HF and MF processes, while the Zr-rich phase promotes the LF processes, in the BSCFZY nanocomposite. For instance, it was found that the ORR rates of BSCF are considerably limited by the poor gas diffusion (Fig. 6c), in good agreement with the results of SEM (Fig. 6b). Indeed, when the microstructures of BSCF and BSCFZY were compared here, BSCFZY demonstrated an enhanced particle-sintering resistance as the particle size of BSCFZY is approximately four times smaller than that of BSCF. The small grain size found in BSCFZY composites can be helpful for facile gas diffusion (Fig. S19†). An additional Brunauer–Emmett–Teller (BET) analysis of the BSCFZY powder sample heat-treated at 1000 °C showed that the surface area is $\sim 1.68 \text{ m}^2 \text{ g}^{-1}$, which is nearly one order of magnitude higher than that of BSCF ($\sim 0.193 \text{ m}^2 \text{ g}^{-1}$), providing further evidence that Zr-BSCFZY exhibits sinter-resistance.

A morphological comparison between BCFZY and BSCF found that the particle size of BCFZY was nearly two times

smaller. Accordingly, in DRT analysis, BCFZY showed a weaker impact on the mass transfer resistance compared to the BSCF sample as expected from the refractory characteristics of this sample (Fig. 6d and S19†).³³ However, the major polarization resistance of BCFZY prevails at the mid-frequency range, which is attributable to the limited electronic conductivity and thus the lack of ability to produce electronically charged oxygen intermediates at the surface. If the two cathode materials are physically mixed, the DRT functions show marginal improvements during both the MF and LF processes (Fig. 6e), whereas the most pronounced enhancements are only accomplished after BSCFZY self-assembles to form sub-microscale composites (Fig. 6f). The results indicate that the formation of an intimately dispersed nano-architecture as prompted from the self-assembly process is the key to achieve tailored characteristics favorable for the ORR process.

Surface exchange and bulk diffusion are closely related to the ORR rates as well. Accordingly, electrical conductivity relaxation is conducted between $pO_2 = 0.21$ and 1 atm to measure the bulk diffusion coefficient (D_{chem}) and surface exchange coefficient (k_{chem}) of BSCFZY (Fig. S20,† electronic conductivity of BSCFZY is shown in Fig. S21†). Significantly, the measured k_{chem} values of BSCFZY are several orders of magnitude higher than those reported for BSCF and BCFZY samples. For instance, the reported k_{chem} value at 450 °C for BCFZY is $\sim 1 \times 10^{-4} \text{ cm s}^{-1}$, and that for BSCF is $\sim 5 \times 10^{-5} \text{ cm s}^{-1}$, whereas the value observed for BSCFZY is $\sim 7.87 \times 10^{-3} \text{ cm s}^{-1}$, which is 78.7 and 157.4 times higher, respectively.²⁷

To investigate in detail the reason for the performance enhancement in BSCFZY, O_2 temperature-programmed-desorption (O_2 -TPD) tests were subsequently carried out in an effort to observe the dynamic process of oxygen adsorption and desorption on perovskite oxides of both BSCFZY and BSCF (Fig. S22†). To this end, the respective 100 mg powders were put under 50 ml min^{-1} He gas in the temperature range of 50–900 °C, with a ramping rate of $10 \text{ }^\circ\text{C min}^{-1}$. The resulting TCD

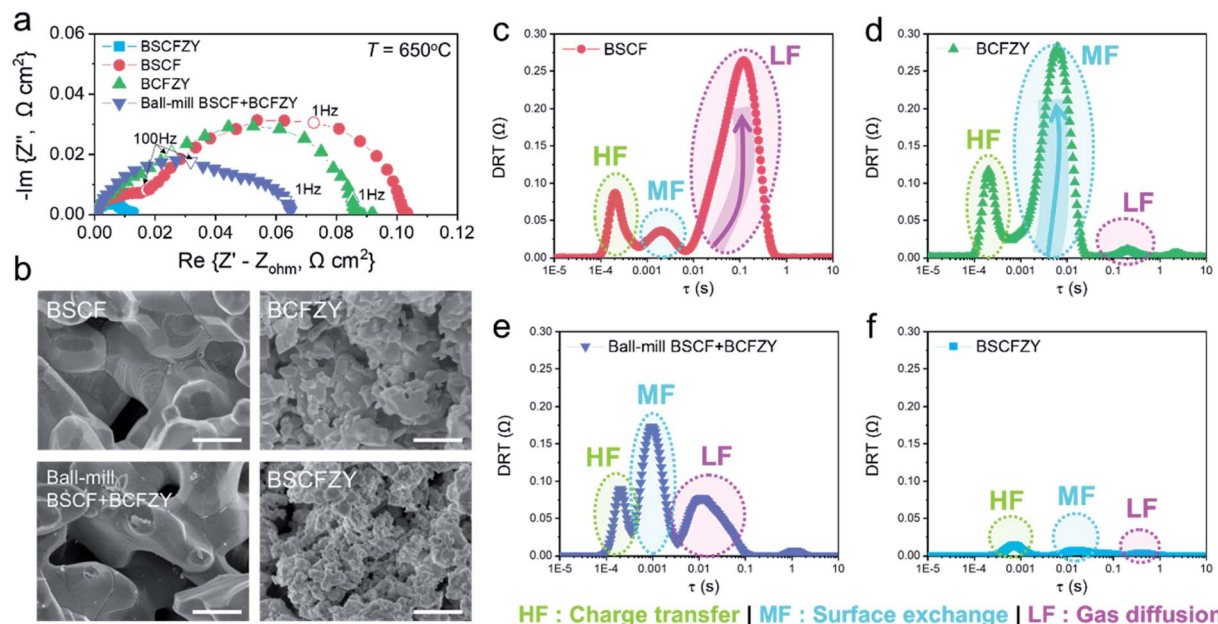


Fig. 6 (a) Comparison of electrochemical impedance spectroscopy (EIS) outcomes of $\text{Ba}_{0.5}\text{Sr}_{0.5}\text{Co}_{0.6}\text{Fe}_{0.2}\text{Zr}_{0.1}\text{Y}_{0.1}\text{O}_{3-\delta}$ (BSCFZY), $\text{Ba}_{0.5}\text{Sr}_{0.5}\text{Co}_{0.8}\text{Fe}_{0.2}\text{O}_{3-\delta}$ (BSCF), $\text{BaCo}_{0.4}\text{Fe}_{0.4}\text{Zr}_{0.1}\text{Y}_{0.1}\text{O}_{3-\delta}$ (BCFZY), and ball-milled BSCF + BCFZY porous cathodes at 650 °C. (b) Scanning electron microscope (SEM) characterization of the surface morphologies of BSCF, BCFZY, ball-milled BSCF + BCFZY and BSCFZY cathodes. Scale bar = 1 μm . The distribution of relaxation time (DRT) analysis results of (c) BSCF, (d) BCFZY, (e) ball-milled BSCF + BCFZY and (f) BSCFZY samples at 650 °C.

signals were recorded using an AutoChem II 2920 device (Micromeritics).

O_2 -TPD provides useful information about oxygen mobility in oxides.^{27,50} Notably, perovskite oxides are known to desorb two types of oxygen; the first is α -oxygen, which originates from the weakly adsorbed oxygen species on the surface in a relatively low-temperature region, and the second is β -oxygen, which originates from the tightly bonded lattice oxygen released at high temperatures.^{29,51} Accordingly, two distinctive peaks were readily identified in BSCFZY and BSCF. Notably, the BSCFZY composite shows the initial desorption temperature and peak temperature of α -oxygen at approximately 150 and 275 °C, respectively, lower than those in BSCF (186 and 279 °C). Significantly, the ratio of α -oxygen to β -oxygen (α -oxygen/ β -oxygen) is found to be much higher in BSCFZY (BSCFZY: 1.95, BSCF: 0.33). This provides qualitative evidence for the faster surface oxygen exchange (k_{chem}) found in BSCFZY due to the larger amounts of weakly bonded surface oxygen species available at the perovskite surface.

Additionally, the initial desorption temperature and peak temperature of β -oxygen found in the BSCFZY composite are approximately 470 and 594 °C, respectively, which are far lower than those in BSCF (500 and 710 °C). The faster activation of lattice oxygen in the bulk perovskite crystal may stem from the superior diffusivity (D_{chem}) found in the BSCFZY composite. Due to the substitution of Co^{3+} by the larger Zr^{4+} and Y^{3+} cations,⁵² the BSCFZY composite shows larger lattice parameters (Co-BSCFZY: 4.01 Å and Zr-BSCFZY: 4.13 Å) than BSCF (3.98 Å)⁵³ and thus exhibits a larger free volume, commonly associated with increased oxygen mobility and decreased activation

energy in perovskites.^{33,54} Accordingly, these results suggest the superior oxygen mobility in BSCFZY composites.

Next, the feasibility of the BSCFZY composite as a SOFC cathode is assessed through single cell tests. First, $\text{NiO-Gd}_{0.1}\text{-Ce}_{0.9}\text{O}_{2-\delta}$ (GDC10) powder is die-pressed to form anode pellets. After light sintering at 950 °C, the GDC20 electrolyte is sequentially deposited onto the anode support by a particle suspension coating process. This is followed by 1450 °C sintering for five hours, to prepare a Ni-GDC10|GDC20 anode-electrolyte bilayer. The cathode is then screen-printed onto the electrolyte and fired at 900 °C to complete the single-cell fabrication process. Fig. 7a shows a cross-sectional SEM image describing the microstructure of the single cell with a configuration of Ni-GDC10|GDC20|BSCFZY. The resulting cathode is approximately 30 μm thick, which is tightly bonded to the electrolyte (thickness: $\sim 13 \mu\text{m}$), indicating good thermal compatibility between the BSCFZY cathode and the GDC20 electrolyte. Not surprisingly, the BSCFZY cathode reveals a nice cathode microstructure which consists of nano-sized grains (Fig. 7b), presumably due to the sinter-resistive characteristic originating from the Zr-BSCFZY phase. Fig. 7c shows typical I - V and I - P curves of button cells using H_2 as the fuel and synthetic air as the oxidant. Accordingly, the cells delivered superior peak power density outcomes of ~ 1.29 and 1.10 W cm^{-2} at 650 and 600 °C, highlighting the excellent outlook of the newly developed cathode achieved *via* the self-assembly process (the EIS of the single cell is measured and presented in Fig. S23†).

The long-term stability of the BSCFZY porous cathode was then assessed with another single cell based on the SDC electrolyte. The microstructure of the SDC-based single cell is

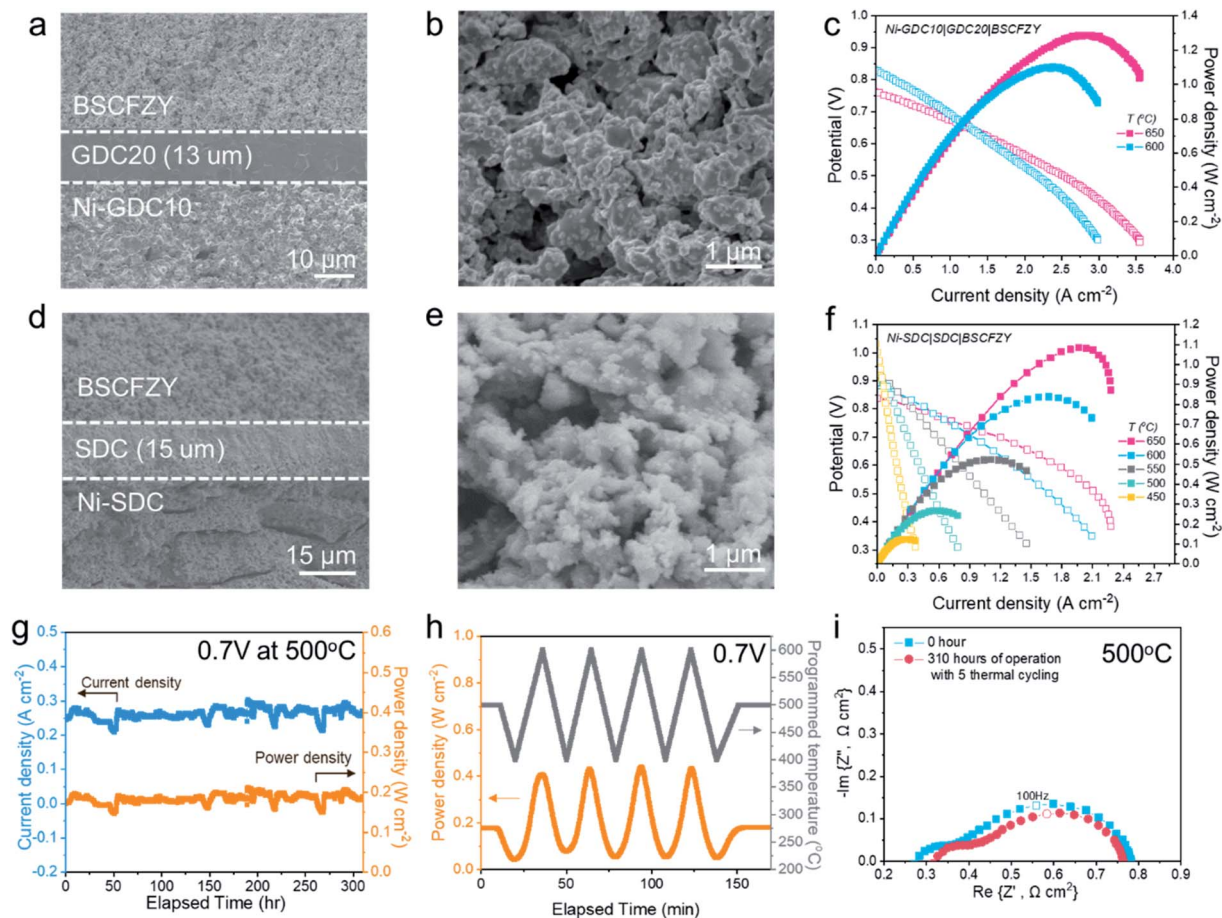


Fig. 7 Performance demonstration with button cells: (a) cross-sectional scanning electron microscope (SEM) image of a Ni-Gd_{0.1}Ce_{0.8}O_{2-δ} (GDC)|Gd_{0.2}Ce_{0.8}O_{2-δ} (GDC20)|Ba_{0.5}Sr_{0.5}Co_{0.6}Fe_{0.2}Zr_{0.1}Y_{0.1}O_{3-δ} (BSCFZY) single cell. (b) Corresponding BSCFZY cathode surface morphology applied to the GDC-based single cell (c) *I*-*V* and *I*-*P* characterization of GDC-based button cells using BSCFZY as the cathode material. (d) Cross-sectional scanning electron microscope (SEM) image of a Ni-Sm_{0.2}Ce_{0.8}O_{2-δ} (SDC)|SDC|BSCFZY single cell. (e) SEM characterization of the surface morphology of the BSCFZY cathode applied to the SDC-based single cell after 310 hours of operation coupled with five thermal cycles. (f) *I*-*V* and *I*-*P* characterization of SDC-based button cells using BSCFZY as the cathode material. (g) Long-term stability measurement of a SDC-based single cell under 0.7 V operation at 500 °C. (h) Thermal cycling of a SDC-based single cell between ~400 and ~600 °C. A constant voltage of 0.7 V is applied during the cycling process. (i) Comparison of the impedance spectra of SDC20-based single cells measured before and after 310 hours of long-term operation with five thermal cycles.

similar to that of the GDC-based cell (Fig. 7d and e) but with a slightly thicker electrolyte layer (~15 μm). The *I*-*V* characterization of the corresponding cell in the temperature range from 450 to 650 °C is shown in Fig. 7f (the EIS of the single cell is measured and presented in Fig. S24 and Table S3†). For an extended duration of ~310 hours of operation under a constant voltage load of 0.7 V at 500 °C, the cell exhibited no noticeable degradation, indicating the exceptional stability provided by the nano-composite cathode (Fig. 7g).

While it is seldom reported, thermal cycling capability is also of paramount importance to ascertain for SOFCs to penetrate deeply into the market. Specifically, under accidental circumstances when the SOFC experiences a sudden temperature drop likely due to a shut-down event, or when a rapid start-up process is needed for an urgent power supply, wild thermal stress will be loaded onto the SOFC and the prevention of cell failure will crucially depend on the TEC mismatch between the cathode

and the electrolyte. To test this, the cell here was put through five rapid ramping cycles between ~400 and ~600 °C with heating and cooling rates of ~14 °C min⁻¹ (Fig. 7h). Significantly, upon the completion of the cycling process, the cell fully recovered its performance capabilities, indicating the adequate thermomechanical compatibility of the BSCFZY cathode with the SDC electrolyte (Fig. 7i). In addition to the intrinsically low TEC value, here we presume that the self-assembly process forms *in situ* generated nanoscale interconnections with strong physical linking effects which may alleviate the expansion of the composite.⁴¹ In addition, the residual nano-pores could also serve to suppress the thermal stress, thereby facilitating an excellent thermomechanical compatibility with SOFC electrolytes.^{55,56} A chemical compatibility test between SDC and BSCFZY was further conducted *via* powder XRD by annealing the SDC-BSCFZY mixture powder at 600 °C for ten hours (Fig. S25†). The XRD profiles of the composite revealed that no

secondary phase arose after high-temperature annealing, implying the reasonable chemical compatibility between electrolytes and developed cathodes.

Finally, we prepare a table of SOFC performance outcomes based on self-assembled composite cathodes to provide a clear comparison (Table S4†). The table shows that our work demonstrates the highest values ever reported, and along with their exceptional durability and thermal cycling capability, our new cathodes are highly promising for high-performance SOFCs to be operated at low-to-intermediate temperatures.

3 Conclusion

In summary, a highly efficient and robust nano-composite, BSCFZY, is showcased here to demonstrate marked performance in SOFCs. BSCFZY self-assembles to produce two discrete phases, where the stable Zr-rich phase prevents the undesirable thermal aggregation of Co-rich phases, hence improving the gas diffusion, while the more electronically conductive Co-rich phase allows sufficient charge carriers for the Zr-rich phase at its perimeter to facilitate accelerated electrocatalysis. Through these synergetic interactions across the nano-scale interface, the resulting multi-phase catalyst enabled an exceptional ASR of $\sim 0.013 \Omega \text{ cm}^2$ at 650°C , a superior power output of $\sim 1.10 \text{ W cm}^{-2}$ at 600°C , durable operation for more than 310 hours at 500°C , and complete rapid ramping cycles without notable degradation, thus highlighting the superiority of the developed materials. Moreover, the succinct preparation of such complex oxides achieved with a single calcination process represents a modest leap forward for advanced and cost-effective SOFC cathode designs for the future.

4 Experimental section

4.1 Material synthesis

The $\text{Ba}_{0.5}\text{Sr}_{0.5}\text{Co}_{0.6}\text{Fe}_{0.2}\text{Zr}_{0.1}\text{Y}_{0.1}\text{O}_{3-\delta}$ (BSCFZY) composite is prepared through a sol-gel method. Stoichiometric amounts of high-purity barium nitrate ($\text{Ba}(\text{NO}_3)_2$, Alfa Aesar), strontium nitrate ($\text{Sr}(\text{NO}_3)_2$, Sigma-Aldrich), cobalt nitrate hexahydrate ($\text{Co}(\text{NO}_3)_2 \cdot 6\text{H}_2\text{O}$, Alfa Aesar), iron nitrate nonahydrate ($\text{Fe}(\text{NO}_3)_3 \cdot 9\text{H}_2\text{O}$, Sigma-Aldrich), a zirconyl nitrate solution (35 wt% of $\text{ZrO}(\text{NO}_3)_2$ in nitric acid, Sigma-Aldrich), and yttrium nitrate hexahydrate ($\text{Y}(\text{NO}_3)_3 \cdot 6\text{H}_2\text{O}$, Sigma-Aldrich) were dissolved in D.I. water with complexing agents ethylenediaminetetraacetic acid (EDTA) and citric acid. The molar ratio of the metal salts, EDTA, and citric acid was 1 : 1 : 2. $\text{NH}_3 \cdot \text{H}_2\text{O}$ was used to adjust the pH value to approximately 9. The solution is then heated to 80°C to evaporate the excessive water. Subsequently, the obtained gel was pre-heated in a heating mantle at 450°C for three hours. The powders were lightly crushed and calcined at 1000°C for five hours to obtain self-assembled perovskites. $\text{Ba}_{0.5}\text{Sr}_{0.5}\text{Co}_{0.6}\text{Fe}_{0.2}\text{Ce}_{0.1}\text{Y}_{0.1}\text{O}_{3-\delta}$ (BSCFCY) and $\text{BaCo}_{0.4}\text{Fe}_{0.4}\text{Zr}_{0.1}\text{Y}_{0.1}\text{O}_{3-\delta}$ (BCFZY) were obtained in a similar manner. $\text{Ba}_{0.5}\text{Sr}_{0.5}\text{Co}_{0.8}\text{Fe}_{0.2}\text{O}_{3-\delta}$ (BSCF) powder was purchased from Kceracell Co., Ltd. The physically mixed ball-milled BSCFZY composite was obtained by mixing 9 g of BSCF with 1 g of BCFZY.

4.2 Physical characterization

The crystal structure of the synthesized powder was analyzed by high-resolution X-ray diffraction (X'Pert-PRO MRD). Cs-corrected scanning transmission electron microscopy (JEOL) was used to characterize the two different phases co-existing in the self-assembled perovskites. The lattice expansion and the corresponding thermal expansion co-efficient (TEC) were analyzed using a high-temperature X-ray diffractometer (D/MAX-2500, Rigaku). The pelletized sample was loaded into the chamber, and the intensities were collected from room temperature to 700°C . The heating rate of the sample was $5^\circ \text{C min}^{-1}$ with a resting time of five-minute before each scan. The scan speed was 4° min^{-1} with a step size of 0.01° . The surface morphologies of the single cells were characterized by using a SEM (Hitachi S-4800). Raman spectroscopy measurements were conducted using an ARAMIS dispersive Raman spectrometer (Horiba Jobin Yvon, France). Raman spectra were recorded using 514 nm excitation laser lines. The Brunauer-Emmett-Teller (BET) analysis was conducted using a TriStar II 3020 (Micromeritics). Before conducting the BET analysis, the powders of BSCF and BSCFZY were heat-treated at 1000°C for one hour.

The as-synthesized BSCFZY nanopowder was electro-deposited on a Ni matrix using the process reported by Kim *et al.* for enabling APT analysis.⁵⁷ APT measurements were conducted using a CAMECA LEAP 4000X HR instrument in a pulsed-laser mode at a pulse frequency of 100 kHz, laser pulse energy of 80 pJ, base temperature of 57 K, and evaporation rate of 0.003 atoms per pulse. Needle-shaped specimens for APT analysis were prepared with ultra-high resolution focused ion beam (Helios G4, FEI) using the standard lift-out protocol.⁵⁸ APT data were analyzed using IVAS 3.8.4 software developed by CAMECA instruments.

4.3 Fabrication of the symmetric cell and button cell

To evaluate the area specific resistance of the developed cathode materials, the configuration of symmetric cells (electrode|SDC|electrode) was devised. First, the SDC powders (fuel cell materials) were dry-pressed in a square steel die and sintered at 1450°C for five hours to form a dense electrolyte pellet. The electrode materials were ball-milled with an ink vehicle (fuel cell materials) in a weight ratio of 1 : 1 for 24 hours with extra ethanol added to a Nalgene bottle. The solution was then dried in an 80°C oven overnight to dry the excess ethanol. Subsequently, the electrode slurry was screen-printed onto both sides of the SDC pellets and fired at 900°C for two hours to complete the symmetric cell fabrication process. Silver paste was applied to the electrode as the current collector.

Anode-supported single cells were prepared to conduct the fuel cell measurements. Anode powder of NiO, an electrolyte powder (SDC, GDC10 from Fuel cell materials), and starch at a weight ratio of 6 : 4 : 1 were initially ball-milled to obtain the anode substrate. The anode powders were pressed in a square steel die and pre-heated at 950°C for one hour in ambient air to heat the fugitive pore-formers of the starch. Atop the anode substrate, the electrolyte slurry was drop-coated. The electrode slurry was prepared by suspending the electrolyte powders in an

organic binder composed of polyvinylpyrrolidone (PVP, Alfa Aesar), butyl benzyl phthalate (Alfa Aesar), triethanolamine (Alfa Aesar), and terpineol (Alfa Aesar). The resulting anode-electrolyte bilayer was sintered at 1450 °C for five hours to densify the electrolyte. Finally, the electrode was screen-printed onto the electrolyte sides to complete the fabrication of the single cell. Two types of single cells (Ni-SDC|SDC|BSCFZY and Ni-GDC10|GDC20|BSCFZY) were used to demonstrate the fuel cell performance. The long-term stability measurements conducted here were based on the Ni-SDC|SDC|BSCFZY cell. Silver paste was used as the current collector.

4.4 Electrochemical measurements

The electrochemical impedance spectroscopy (EIS) results of the cathode symmetric cell were obtained by AC impedance measurements using a Biologics VSP-300 device as the workstation (OCV, 1 MHz to 0.01 Hz) in the temperature range of 450–650 °C. The cells were placed in an alumina tube in contact with a pseudo-four-configuration probe with a platinum wire. The mixture gases (O₂-Ar) were flowed into the tube with digital mass flow controllers. The *I-V* and *I-P* curves were collected using the Biologics VSP-300 device at 0.03 V s⁻¹. An in-lab-constructed fuel-cell testing station operating within the temperature range of 450–650 °C was utilized. During the single cell test, H₂ gas was flowed into the anode side at a flow rate of 75 ml min⁻¹, while 75 ml of synthetic air (N₂: 79%, O₂: 21%) min⁻¹ was fed into the cathode side. DRT analyses were conducted with DRT tools and software obtained from Francesco Ciucci's group.^{59–61}

Author contributions

W. J. conceived and supervised the project. J. H. K. fabricated materials, performed the electrochemical testing, XRD, TEM, and Raman spectroscopy. K. J. conducted APT sample preparation and analysis. D. L. executed electrical conductivity measurements and ECR. D. O and S. A. assisted powder fabrication and XRD analysis. H. K. aided the APT sample preparation. J. S. undertook XPS analysis. J. H. K., P. C. and W. J. contributed to the writing of the paper.

Conflicts of interest

The authors declare no conflict of interests.

Acknowledgements

This work was supported by the Korea Institute of Energy Technology Evaluation and Planning (KETEP) and the Ministry of Trade, Industry & Energy (MOTIE) of the Republic of Korea (No. 2019A030202360) and Nano Material Technology Development Program through the National Research Foundation of Korea (NRF) funded by the Ministry of Science and ICT (2021M3H4A1A01079300).

References

- 1 N. W. Kwak, S. J. Jeong, H. G. Seo, S. Lee, Y. Kim, J. K. Kim, P. Byeon, S.-Y. Chung and W. Jung, In situ synthesis of supported metal nanocatalysts through heterogeneous doping, *Nat. Commun.*, 2018, **9**(1), 4829.
- 2 Y. Wang, Z. Wang, C. Jin, C. Li, X. Li, Y. Li, R. Yang and M. Liu, Enhanced overall water electrolysis on a bifunctional perovskite oxide through interfacial engineering, *Electrochim. Acta*, 2019, **318**, 120–129.
- 3 Y.-F. Sun, Y.-L. Yang, J. Chen, M. Li, Y.-Q. Zhang, J.-H. Li, B. Hua and J.-L. Luo, Toward a rational photocatalyst design: a new formation strategy of co-catalyst/semiconductor heterostructures via in situ exsolution, *Chem. Commun.*, 2018, **54**(12), 1505–1508.
- 4 J. H. Kim, J. K. Kim, J. Liu, A. Curcio, J.-S. Jang, I.-D. Kim, F. Ciucci and W. Jung, Nanoparticle Ex-solution for Supported Catalysts: Materials Design, Mechanism and Future Perspectives, *ACS Nano*, 2020, **15**(1), 81–110.
- 5 M. Cargnello, V. V. Doan-Nguyen, T. R. Gordon, R. E. Diaz, E. A. Stach, R. J. Gorte, P. Fornasiero and C. B. Murray, Control of metal nanocrystal size reveals metal-support interface role for ceria catalysts, *Science*, 2013, **341**(6147), 771–773.
- 6 R. Subbaraman, D. Tripkovic, D. Strmcnik, K.-C. Chang, M. Uchimura, A. P. Paulikas, V. Stamenkovic and N. M. Markovic, Enhancing hydrogen evolution activity in water splitting by tailoring Li+-Ni(OH) 2-Pt interfaces, *Science*, 2011, **334**(6060), 1256–1260.
- 7 S. Joo, A. Seong, O. Kwon, K. Kim, J. H. Lee, R. J. Gorte, J. M. Vohs, J. W. Han and G. Kim, Highly active dry methane reforming catalysts with boosted in situ grown Ni-Fe nanoparticles on perovskite via atomic layer deposition, *Sci. Adv.*, 2020, **6**(35), eabb1573.
- 8 Y. Chen, Y. Choi, S. Yoo, Y. Ding, R. Yan, K. Pei, C. Qu, L. Zhang, I. Chang and B. Zhao, A Highly Efficient Multi-phase Catalyst Dramatically Enhances the Rate of Oxygen Reduction, *Joule*, 2018, **2**(5), 938–949.
- 9 M. Liu, M. E. Lynch, K. Blinn, F. M. Alamgir and Y. Choi, Rational SOFC material design: new advances and tools, *Mater. Today*, 2011, **14**(11), 534–546.
- 10 Y. Chen, B. deGlee, Y. Tang, Z. Wang, B. Zhao, Y. Wei, L. Zhang, S. Yoo, K. Pei, J. H. Kim, Y. Ding, P. Hu, F. F. Tao and M. Liu, A robust fuel cell operated on nearly dry methane at 500 °C enabled by synergistic thermal catalysis and electrocatalysis, *Nat. Energy*, 2018, **3**(12), 1042–1050.
- 11 E. D. Wachsman and K. T. Lee, Lowering the temperature of solid oxide fuel cells, *Science*, 2011, **334**(6058), 935–939.
- 12 S. Choi, Electrochemical properties of Sr-doped layered perovskite as a promising anode material for direct hydrocarbon SOFCs, *J. Korean Ceram. Soc.*, 2020, **57**(4), 409–415.
- 13 X. Zhang, Y. Jiang, X. Hu, L. Sun and Y. Ling, High Performance Proton-Conducting Solid Oxide Fuel Cells

- with a Layered Perovskite GdBaCuCoO_{5+x} Cathode, *Electron. Mater. Lett.*, 2018, **14**(2), 147–153.
- 14 J. H. Kim, M. Liu, Y. Chen, R. Murphy, Y. Choi, Y. Liu and M. Liu, Understanding the Impact of Sulfur Poisoning on the Methane-Reforming Activity of a Solid Oxide Fuel Cell Anode, *ACS Catal.*, 2021, **11**(21), 13556–13566.
 - 15 Z. Gao, L. V. Mogni, E. C. Miller, J. G. Railsback and S. A. Barnett, A perspective on low-temperature solid oxide fuel cells, *Energy Environ. Sci.*, 2016, **9**(5), 1602–1644.
 - 16 Y. Chen, S. Yoo, Y. Choi, J. H. Kim, Y. Ding, K. Pei, R. Murphy, Y. Zhang, B. Zhao, W. Zhang, H. Chen, Y. Chen, W. Yuan, C. Yang and M. Liu, A highly active, CO₂-tolerant electrode for the oxygen reduction reaction, *Energy Environ. Sci.*, 2018, **11**(9), 2458–2466.
 - 17 S. Yoo, A. Jun, Y. W. Ju, D. Odkhuu, J. Hyodo, H. Y. Jeong, N. Park, J. Shin, T. Ishihara and G. Kim, Development of Double-Perovskite Compounds as Cathode Materials for Low-Temperature Solid Oxide Fuel Cells, *Angew. Chem., Int. Ed.*, 2014, **53**(48), 13064–13067.
 - 18 D. Neagu, G. Tsekouras, D. N. Miller, H. Ménard and J. T. Irvine, In situ growth of nanoparticles through control of non-stoichiometry, *Nat. Chem.*, 2013, **5**(11), 916–923.
 - 19 J. H. Kim, J. K. Kim, H. G. Seo, D. K. Lim, S. J. Jeong, J. Seo, J. Kim and W. Jung, Ex-Solved Ag Nanocatalysts on a Sr-Free Parent Scaffold Authorize a Highly Efficient Route of Oxygen Reduction, *Adv. Funct. Mater.*, 2020, 2001326.
 - 20 B. Zhao, L. Zhang, D. Zhen, S. Yoo, Y. Ding, D. Chen, Y. Chen, Q. Zhang, B. Doyle and X. Xiong, A tailored double perovskite nanofiber catalyst enables ultrafast oxygen evolution, *Nat. Commun.*, 2017, **8**, 14586.
 - 21 Y. Chen, Y. Bu, Y. Zhang, R. Yan, D. Ding, B. Zhao, S. Yoo, D. Dang, R. Hu and C. Yang, A highly efficient and robust nanofiber cathode for solid oxide fuel cells, *Adv. Energy Mater.*, 2017, **7**(6), 1601890.
 - 22 J. G. Lee, J. H. Park and Y. G. Shul, Tailoring gadolinium-doped ceria-based solid oxide fuel cells to achieve 2 W cm⁻² at 550 C, *Nat. Commun.*, 2014, **5**(1), 1–10.
 - 23 Y. Song, Y. Chen, M. Xu, W. Wang, Y. Zhang, G. Yang, R. Ran, W. Zhou and Z. Shao, A Cobalt-Free Multi-Phase Nanocomposite as Near-Ideal Cathode of Intermediate-Temperature Solid Oxide Fuel Cells Developed by Smart Self-Assembly, *Adv. Mater.*, 2020, **32**(8), 1906979.
 - 24 J. F. Shin, W. Xu, M. Zanella, K. Dawson, S. N. Savvin, J. B. Claridge and M. J. Rosseinsky, Self-assembled dynamic perovskite composite cathodes for intermediate temperature solid oxide fuel cells, *Nat. Energy*, 2017, **2**(3), 1–7.
 - 25 J. H. Kim, S. Yoo, R. Murphy, Y. Chen, Y. Ding, K. Pei, B. Zhao, G. Kim, Y. Choi and M. Liu, Promotion of Oxygen Reduction Reaction on a Double Perovskite Electrode by a Water-induced Surface Modification, *Energy Environ. Sci.*, 2021, **14**(3), 1506–1516.
 - 26 A. Demont, R. Sayers, M. A. Tsiamtsouri, S. Romani, P. A. Chater, H. Niu, C. Martí-Gastaldo, Z. Xu, Z. Deng and Y. Bréard, Single sublattice endotaxial phase separation driven by charge frustration in a complex oxide, *J. Am. Chem. Soc.*, 2013, **135**(27), 10114–10123.
 - 27 Y. Song, Y. Chen, W. Wang, C. Zhou, Y. Zhong, G. Yang, W. Zhou, M. Liu and Z. Shao, Self-Assembled Triple-Conducting Nanocomposite as a Superior Protonic Ceramic Fuel Cell Cathode, *Joule*, 2019, **3**(11), 2842–2853.
 - 28 H. Qi, Z. Zhao, X. Wang, B. Tu and M. Cheng, Self-assembled cubic-hexagonal perovskite nanocomposite as intermediate-temperature solid oxide fuel cell cathode, *Ceram. Int.*, 2020, **46**(14), 22282–22289.
 - 29 H. Qi, T. Zhang, D. Liu, M. Cheng and B. Tu, Investigation of a self-assembled Sr_{0.74}La_{0.26}CoO_{3-δ}-SrZr_{0.79}Co_{0.21}O_{3-δ} composite with hierarchical structure as intermediate-temperature solid oxide fuel cell cathode, *J. Power Sources*, 2021, **506**, 230230.
 - 30 Y. Chen, Y. Chen, D. Ding, Y. Ding, Y. Choi, L. Zhang, S. Yoo, D. Chen, B. Deglee and H. Xu, A robust and active hybrid catalyst for facile oxygen reduction in solid oxide fuel cells, *Energy Environ. Sci.*, 2017, **10**(4), 964–971.
 - 31 K. T. Lee, A. A. Lidie, H. S. Yoon and E. D. Wachsman, Rational design of lower-temperature solid oxide fuel cell cathodes via nanotailoring of co-assembled composite structures, *Angew. Chem., Int. Ed.*, 2014, **53**(49), 13463–13467.
 - 32 Z. Shao and S. M. Haile, A high-performance cathode for the next generation of solid-oxide fuel cells, *Nature*, 2004, **431**(7005), 170–173.
 - 33 C. Duan, D. Hook, Y. Chen, J. Tong and R. O'Hayre, Zr and Y co-doped perovskite as a stable, high performance cathode for solid oxide fuel cells operating below 500 C, *Energy Environ. Sci.*, 2017, **10**(1), 176–182.
 - 34 J.-I. Jung and D. D. Edwards, X-ray photoelectron study on Ba_{0.5}Sr_{0.5}Co_xFe_{1-x}O_{3-δ} (BSCF: x = 0.2 and 0.8) ceramics annealed at different temperature and pO₂, *J. Mater. Sci.*, 2011, **46**(23), 7415–7422.
 - 35 R. Zohourian, R. Merkle, G. Raimondi and J. Maier, Mixed-conducting perovskites as cathode materials for protonic ceramic fuel cells: understanding the trends in proton uptake, *Adv. Funct. Mater.*, 2018, **28**(35), 1801241.
 - 36 C. Duan, J. Tong, M. Shang, S. Nikodemski, M. Sanders, S. Ricote, A. Almansoori and R. O'Hayre, Readily processed protonic ceramic fuel cells with high performance at low temperatures, *Science*, 2015, **349**(6254), 1321.
 - 37 J. H. Kim, Z.-Y. Chern, S. Yoo, B. M. deGlee, J.-H. Wang and M. Liu, Unraveling the Mechanism of Water-mediated Sulfur Tolerance via Operando Surface Enhanced Raman Spectroscopy, *ACS Appl. Mater. Interfaces*, 2019, **12**(2), 2370–2379.
 - 38 L. Mazzei, D. Rukser, F. Biebl, B. Grimm-Lebsanft, G. Neuber, D. Pergolesi, L. Börjesson, M. A. Rübhausen, J. Andreasson and M. Karlsson, Phonon spectra of pure and acceptor doped BaZrO₃ investigated with visible and UV Raman spectroscopy, *J. Phys.: Condens. Matter*, 2020, **32**(40), 405403.
 - 39 F. Dong, D. Chen, Y. Chen, Q. Zhao and Z. Shao, La-doped BaFeO_{3-δ} perovskite as a cobalt-free oxygen reduction electrode for solid oxide fuel cells with oxygen-ion

- conducting electrolyte, *J. Mater. Chem.*, 2012, **22**(30), 15071–15079.
- 40 E. Y. Pikalova, V. Maragou, A. Demina, A. Demin and P. Tsiakaras, The effect of co-dopant addition on the properties of $\text{Ln}_0.2\text{Ce}_0.8\text{O}_2-\delta$ ($\text{Ln} = \text{Gd}, \text{Sm}, \text{La}$) solid-state electrolyte, *J. Power Sources*, 2008, **181**(2), 199–206.
- 41 Y. Zhang, B. Chen, D. Guan, M. Xu, R. Ran, M. Ni, W. Zhou, R. O'Hayre and Z. Shao, Thermal-expansion offset for high-performance fuel cell cathodes, *Nature*, 2021, **591**(7849), 246–251.
- 42 Y. Chen, J. Shen, G. Yang, W. Zhou and Z. Shao, A single-/double-perovskite composite with an overwhelming single-perovskite phase for the oxygen reduction reaction at intermediate temperatures, *J. Mater. Chem. A*, 2017, **5**(47), 24842–24849.
- 43 S.-W. Baek, J. H. Kim and J. Bae, Characteristics of ABO_3 and A_2BO_4 ($\text{ASm}, \text{Sr}; \text{BCo}, \text{Fe}, \text{Ni}$) samarium oxide system as cathode materials for intermediate temperature-operating solid oxide fuel cell, *Solid State Ionics*, 2008, **179**(27–32), 1570–1574.
- 44 M. Li, K. Chen, B. Hua, J.-l. Luo, W. D. Rickard, J. Li and J. T. Irvine, Smart utilization of cobaltite-based double perovskite cathodes on barrier-layer-free zirconia electrolyte of solid oxide fuel cells, *J. Mater. Chem. A*, 2016, **4**(48), 19019–19025.
- 45 B. Koo, K. Kim, J. K. Kim, H. Kwon, J. W. Han and W. Jung, Sr segregation in perovskite oxides: why it happens and how it exists, *Joule*, 2018, **2**(8), 1476–1499.
- 46 Y. Li, W. Zhang, Y. Zheng, J. Chen, B. Yu, Y. Chen and M. Liu, Controlling cation segregation in perovskite-based electrodes for high electro-catalytic activity and durability, *Chem. Soc. Rev.*, 2017, **46**(20), 6345–6378.
- 47 X. Chen, K. Khor and S. Chan, Identification of O_2 reduction processes at yttria stabilized zirconia|doped lanthanum manganite interface, *J. Power Sources*, 2003, **123**(1), 17–25.
- 48 Z. Jiang, Z. Lei, B. Ding, C. Xia, F. Zhao and F. Chen, Electrochemical characteristics of solid oxide fuel cell cathodes prepared by infiltrating (La, Sr) MnO_3 nanoparticles into yttria-stabilized bismuth oxide backbones, *Int. J. Hydrogen Energy*, 2010, **35**(15), 8322–8330.
- 49 B. Kenney and K. Karan, Impact of nonuniform potential in SOFC composite cathodes on the determination of electrochemical kinetic parameters: a numerical analysis, *J. Electrochem. Soc.*, 2006, **153**(6), A1172.
- 50 Z. Zhang, Y. Zhu, Y. Zhong, W. Zhou and Z. Shao, Anion doping: a new strategy for developing high-performance perovskite-type cathode materials of solid oxide fuel cells, *Adv. Energy Mater.*, 2017, **7**(17), 1700242.
- 51 B. Kayaalp, S. Lee, K. Klauke, J. Seo, L. Nodari, A. Kornowski, W. Jung and S. Mascotto, Template-free mesoporous $\text{La}_0.3\text{Sr}_0.7\text{Ti}_{1-x}\text{Fe}_x\text{O}_{3\pm\delta}$ for CH_4 and CO oxidation catalysis, *Appl. Catal., B*, 2019, **245**, 536–545.
- 52 R. D. Shannon, Revised effective ionic radii and systematic studies of interatomic distances in halides and chalcogenides, *Acta Crystallogr., Sect. A: Cryst. Phys., Diffraction, Theor. Gen. Crystallogr.*, 1976, **32**(5), 751–767.
- 53 H. Wang, C. Tablet, W. Yang and J. Caro, In situ high temperature X-ray diffraction studies of mixed ionic and electronic conducting perovskite-type membranes, *Mater. Lett.*, 2005, **59**(28), 3750–3755.
- 54 M. Mogensen, D. Lybye, N. Bonanos, P. Hendriksen and F. Poulsen, Factors controlling the oxide ion conductivity of fluorite and perovskite structured oxides, *Solid State Ionics*, 2004, **174**(1–4), 279–286.
- 55 W. Uju and I. Oguocha, A study of thermal expansion of Al-Mg alloy composites containing fly ash, *Mater. Des.*, 2012, **33**, 503–509.
- 56 V. V. Ganesh and M. Gupta, Effect of the extent of reinforcement interconnectivity on the properties of an aluminum alloy, *Scr. Mater.*, 2001, **44**(2), 305–310.
- 57 S.-H. Kim, P. W. Kang, O. O. Park, J.-B. Seol, J.-P. Ahn, J. Y. Lee and P.-P. Choi, A new method for mapping the three-dimensional atomic distribution within nanoparticles by atom probe tomography (APT), *Ultramicroscopy*, 2018, **190**, 30–38.
- 58 K. Thompson, D. Lawrence, D. Larson, J. Olson, T. Kelly and B. Gorman, In situ site-specific specimen preparation for atom probe tomography, *Ultramicroscopy*, 2007, **107**(2–3), 131–139.
- 59 F. Ciucci and C. Chen, Analysis of electrochemical impedance spectroscopy data using the distribution of relaxation times: a bayesian and hierarchical bayesian approach, *Electrochim. Acta*, 2015, **167**, 439–454.
- 60 T. H. Wan, M. Saccoccio, C. Chen and F. Ciucci, Influence of the discretization methods on the distribution of relaxation times deconvolution: implementing radial basis functions with DRTtools, *Electrochim. Acta*, 2015, **184**, 483–499.
- 61 M. Saccoccio, T. H. Wan, C. Chen and F. Ciucci, Optimal regularization in distribution of relaxation times applied to electrochemical impedance spectroscopy: ridge and lasso regression methods—a theoretical and experimental study, *Electrochim. Acta*, 2014, **147**, 470–482.